RSC Advances

RSC Publishing

PAPER

View Article Online
View Journal | View Issue

Cite this: *RSC Advances*, 2013, **3**, 3421

Defect-free solvothermally assisted synthesis of microspherical mesoporous $LiFePO_4$/C†

Min-Young Cho,[ab] Kwang-Bum Kim,[b] Jae-Won Lee,[c] Haegyeom Kim,[d] Hyungsub Kim,[d] Kisuk Kang[d] and Kwang Chul Roh*[a]

Received 20th November 2012,
Accepted 21st December 2012

DOI: 10.1039/c2ra22965j

www.rsc.org/advances

Recent studies have shown that the power capability of $LiFePO_4$ is dramatically enhanced by reducing the size of the $LiFePO_4$ particles to nanometer dimensions. Unfortunately, the resulting intrinsically low tap density of the nano-$LiFePO_4$ cathode significantly reduces the volumetric energy density, which is a major hurdle for the successful commercialization of this material. Here, we report the facile synthesis of carbon-coated $LiFePO_4$ ($LiFePO_4$/C) with a mesoporous microspherical morphology *via* a solvothermal process, using ethanol as the sole solvent and in the absence of chelating agents. $LiFePO_4$/C was highly crystalline and exhibited less than 1% anti-site defects, which is important for fast lithium conduction in $LiFePO_4$. $LiFePO_4$/C showed an excellent rate performance (86 mAh g^{-1} at a 20 C rate), a high retention ratio of 100% (140 mAh g^{-1} at a 1 C rate), and a high tap density (1.2 g cm^{-3}). The material is thus suitable for use as a cathode in lithium-ion batteries and for high-power energy storage devices.

Introduction

In recent years, the development of lithium-ion batteries with high power and high energy densities has accelerated because of the miniaturization of portable electronic devices and the introduction of lithium-ion battery powered (hybrid) electric vehicles. Lithium iron phosphate ($LiFePO_4$) is a promising cathode material with advantageous properties such as low cost and toxicity, high theoretical capacity (170 mAh g^{-1}), an enhanced cycle life, and high thermal stability.[1,2] Unfortunately, it exhibits relatively low intrinsic electronic conductivity (10^{-9}–10^{-10} S cm^{-1}) owing to its corner-shared FeO_6 octahedra.[3] Many strategies, such as controlling the particle size by the synthesis of nano-$LiFePO_4$,[4] coating[5] or complexation[6] with conductive carbon, and doping with supervalent cations such as Zr, Ti, Nb, and Mg,[7] have been developed to overcome these drawbacks.

Among these strategies, particle size reduction and carbon coating have proven to be effective in enhancing the high rate performance of this material, as they contributes to the reduction of the diffusion path length,[4,8,9] and the improvement of electronic conductivity.[3,5] To date, the occurrence of anti-site defects in the $LiFePO_4$ crystal structure plays a decisive role in the rate performance of this material. Anti-site defects result from the displacement of the lithium sites by transition metals, which block lithium diffusion through the one-dimensional channel along the [010] direction in $LiFePO_4$ crystal structure, a process known as channel blocking.[10] In turn, this affects the electrochemical performance of the electrode. Qin *et al.*[10] used FTIR data (*i.e.*, the occurrence of red shifts that were consistent with the symmetric P–O stretching vibration in the PO_4 tetrahedron) to demonstrate that ethylene glycol and ethanol, being solvents with low dielectric constants, played an essential role in reducing the concentration of $Fe^{\bullet}_{Li}$ anti-site defects. Other studies[11–13] have proven the existence of $Fe^{\bullet}_{Li}$ + V'_{Li} defects, and studied the effect of reaction temperature and chelating agents using Rietveld refinement (*i.e.*, a different unit cell volume (or decreased lattice parameters) was observed for $LiFePO_4$ prepared using Fe^{2+} as the starting material). Apart from the problems associated with anti-site defects, the benefits of employing nanosized $LiFePO_4$ are counterbalanced by the significantly reduced volumetric energy density due to the intrinsic low tap density of the nanomaterial. Indeed, this remains one of the major challenges for its successful commercialization.

In summary, economically viable $LiFePO_4$ electrodes should exhibit the following properties: (i) a low concentration

[a]*Energy Efficient Materials Team, Energy & Environmental Division, Korea Institute of Ceramic Engineering & Technology, 233-5 Gasan-dong, Guemcheon-gu, Seoul 153-801, Republic of Korea. E-mail: rkc@kicet.re.kr; Fax: +82-2-3282-2475; Tel: +82-2-3282-2463*

[b]*Department of Materials Science & Engineering, Yonsei University, 50 Yonsei-ro, Seodaemun-gu, Seoul 120-749, Republic of Korea*

[c]*Department of Energy Engineering, Dankook University, Cheonan 330-714, Republic of Korea*

[d]*Department of Materials Science and Engineering, Seoul National University, 599 Gwanak-ro, Gwanak-gu, Seoul 151-741, Republic of Korea*

† Electronic supplementary information (ESI) available: XRD patterns of the precursor; FE-SEM image of the precursor prepared using water as the solvent; Rietveld refinements of the XRD patterns; cyclic voltammograms of bare $LiFePO_4$ and $LiFePO_4$/C at varying scan rates. See DOI: 10.1039/c2ra22965j

of anti-site defects, (ii) micron-sized particles, (iii) a reduced path length for lithium ion migration, and (iv) an improved electronic conductivity by a uniform carbon coating. To synthesize carbon-coated $LiFePO_4$ ($LiFePO_4$/C) with the desired properties, we prepared mesoporous spherical $LiFePO_4$ using a simple solvothermal reaction, employing Fe^{3+} salt and ethanol as the starting material and solvent, respectively. The morphology and pore structure of the as-prepared bare $LiFePO_4$ and $LiFePO_4$/C synthesized using this precursor were carefully characterized by X-ray diffraction (XRD) and Fourier transform infrared spectroscopy (FTIR), so as to determine whether using ethanol as the solvent led to a reduced concentration of $Fe^{\bullet}_{Li}$ anti-site defects. The effect of pore structure and the uniform carbon coating on the electrochemical performance of bare $LiFePO_4$ and $LiFePO_4$/C was also examined.

Experimental

Preparation of $LiFe(PO_4)(OH)$ precursor

Stoichiometric amounts of 0.028 mol lithium acetate hydrate ($CH_3COOLi{\cdot}2H_2O$), iron(III) nitrate hydrate ($Fe(NO_3)_3{\cdot}9H_2O$), and phosphoric acid (85 wt%, H_3PO_4) were dissolved in 40 mL absolute ethanol. The mixture was stirred for 0.5 h and transferred to a 100 mL Teflon-lined autoclave. The autoclave was sealed and heated to 160 °C for 2 h. After cooling to room temperature, the precursor was obtained by filtration, washed with distilled water, and dried in air at 80 °C for 24 h.

Preparation of bare $LiFePO_4$ and $LiFePO_4$/C

To obtain the bare $LiFePO_4$, the precursor was heated to 700 °C (heating and cooling rates: 2 °C min^{-1}) for 12 h in a hydrogen–argon mixture (5 vol% H_2) at a flow rate of 300 mL min^{-1}, to reduce Fe^{3+} to Fe^{2+}. Carbon-coated $LiFePO_4$ ($LiFePO_4$/C) was obtained by mixing the preheated (400 °C for 12 h) precursor and citric acid (precursor : citric acid weight ratio = 1 : 0.4) in absolute ethanol. The mixture was stirred at a constant temperature of 90 °C until the ethanol evaporated. The mixture was then treated following the procedure described for the preparation of bare $LiFePO_4$.

Characterization

The morphology and particle size distributions of the synthesized samples were investigated using field emission scanning microscopy (FE-SEM, JEOL JSM-6700F). The crystalline phases were analyzed using X-ray diffraction (XRD, Rigaku D/Max-2500/PC) in the 2θ range 10–100°, 0.02 steps/4 s, using Cu Kα radiation (λ = 1.54 Å), and the crystallite size (D) was calculated using the Scherrer equation. XRD data were refined by the Rietveld method using FullProf software. Fourier transform infrared spectroscopy (FTIR) (FT/IR 4200) was performed using KBr pellets. X-ray photoelectron spectroscopy (XPS) was performed using a PHI 5000 VersaProbe™ spectrometer with Al Kα radiation ($h\upsilon$ = 1486.6 eV) to analyze the valence state of the samples. The content and thickness of the carbon coated on $LiFePO_4$/C was measured using a carbon–sulfur determinator (LECO Co., CS600) and a high-resolution transmission electron microscope (HR-TEM, JEM 2000EX, JEOL), respectively. Specific surface area and pore distributions were measured using the Brunauer–Emmett–Teller method (BET, BELSORP-Mini II). Pore sizes were calculated using the Barrett–Joyner–Halenda (BJH) method.

Electrochemical measurements

The electrochemical properties of the samples were measured using a coin cell (CR2016). A cathode electrode was produced by coating a slurry of 80 wt% active material ($LiFePO_4$), 15 wt% conductive additive (SUPER P® carbon black), and 5 wt% binder (polyvinylidene fluoride) onto an aluminum-foil current collector. Lithium metal was used as the anode electrode. The coin cell was assembled in an argon-filled glove box. The separator and electrolyte used were microporous polyethylene and 1.0 M $LiPF_6$ in ethylene carbonate (EC)–ethyl methyl carbonate (EMC) (EC : EMC = 1 : 2 by volume), respectively. To reduce the irreversible capacity of the electrode, the active material was impregnated with electrolyte using a vacuum apparatus. Galvanostatic charge and discharge tests were performed on the as-prepared cell and a conventional Li/Li^+ cell in the potential range 2.0–4.5 V. Cyclic voltammetry (CV, Bio-Logic, VSP) was performed on the cells at various scan rates in a potential range of 0.2–1 mV s^{-1}. The CV data were used to estimate the diffusion coefficient of Li^+. All electrochemical tests were conducted at room temperature.

Results and discussion

The FE-SEM image in Fig. 1(a) shows the morphology of the $LiFePO_4$ precursor. Secondary particles with a spherical morphology, consisting of numerous nanosized primary particles, are clearly visible (Fig. 1(a), inset). The formation of secondary particles with spherical morphology can be explained by the dissolution–precipitation process that governs crystal growth (see further).[15,17] The particles have a narrow size distribution (~1.5–2 μm), despite the relatively short synthesis time (2 h). The size distribution observed is smaller than those for previously reported microspherical $LiFePO_4$ particles produced using coprecipitation and hydrothermal reactions.[14,15] This may result from the fact that we employed ethanol as the sole solvent in the solvothermal synthesis, which displays a relatively low dielectric constant (ε_{water} = 80.3, $\varepsilon_{ethanol}$ = 25.0 at 20 °C).

The relationship between dielectric constant and nuclei radii (*i.e.*, particle size) can be expressed as follows:[16]

in which $$1/r = A + B\varepsilon^{-1} \quad (1a)$$

and $$A = (kT\rho/2m\gamma)\ \ln C \quad (1b)$$

$$B = (\rho z_+ z_- e^2)/8\pi m\gamma\varepsilon_0\ (r_+ + r_-) \quad (1c)$$

Here, r is the radius of stable nuclei, ε is the dielectric constant, ρ is the density of the solute molecule, C is the solute concentration, m is the weight of the solute molecule, γ is interfacial energy between the solute and the solution phase, e

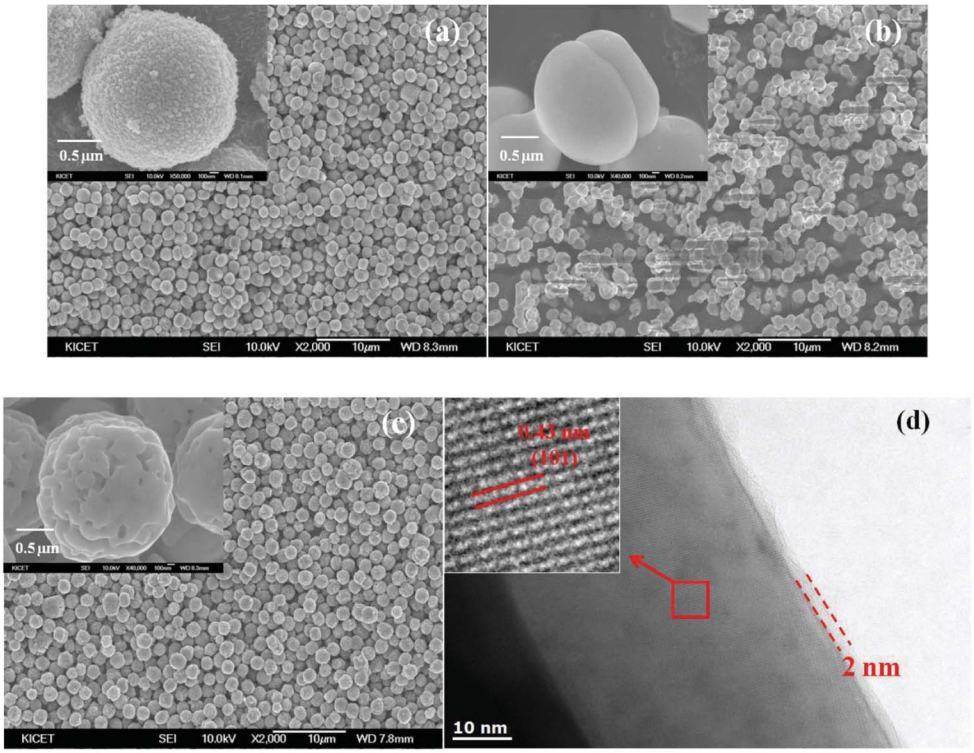

Fig. 1 FE-SEM images of (a) uniformly sized $LiFePO_4$ precursor particles synthesized using the 2 h solvothermal process with ethanol as the solvent, (b) nonporous bare $LiFePO_4$ after heat treatment of the precursor material without the addition of citric acid, and (c) porous $LiFePO_4$/C after heat treatment of the preheated precursor and the addition of citric acid. $LiFePO_4$/C particles display a similar size and morphology to that of the precursor. (d) High-magnification HR-TEM image of $LiFePO_4$/C. The inset is an electron diffraction pattern of a selected area. The $LiFePO_4$/C particles show a porous structure with an amorphous carbon coating ~2 nm thick.

is the elementary charge (1.602×10^{-19} C), z_+ and z_- are the valences of the charged ions, r_+ and r_- are the radii of the charged ions, and ε_0 is the permittivity of the vacuum. In principle, A and B can be regarded as constants; when a solvent with a low dielectric constant (such as ethanol) is used, the reaction easily reaches high supersaturation, accelerating the nucleation rate and decreasing the nuclei radii proportionally with decreasing the dielectric constant of the solvent. At the same time, the rate of the reaction increases because the boiling point of ethanol (78.3 °C) is lower than that of water (100 °C), and hence the vapor pressure of ethanol ($\sim$1.25 MPa) is more than twice that of water ($\sim$0.61 MPa).

The chelating effect of ethanol is demonstrated by XRD analysis (Fig. S1†) of the precursors, synthesized using either water or ethanol as the solvent, where water gives rise to the $Fe_5(PO_4)_4(OH)_3{\cdot}2H_2O$ phase (*i.e.*, no Li composites present) and ethanol gives rise to highly crystalline $LiFe(PO_4)(OH)$ phases, after only 2 h reaction time. The precursor particles, prepared using water as the solvent, furthermore show irregular shapes and a relatively large size (>3 μm) owing to the simultaneous growth and agglomeration of the primary particles (Fig. S2†). Thus, we concluded that ethanol acts not only as a solvent but also as a chelating agent, as was previously observed for ethylene glycol.[17] Fig. 1(b) and (c) show the FE-SEM images of the bare $LiFePO_4$ and $LiFePO_4$/C particles after heat treatment. The $LiFePO_4$/C particles exhibit a similar size and morphology to the precursor. The most noticeable difference is that the $LiFePO_4$/C particles exhibit macropores on their outer surfaces, while the bare $LiFePO_4$ particles show a decreased size and their surface is solid because of undesired particle aggregation and growth during the high-temperature treatment. The HR-TEM image of $LiFePO_4$/C is shown in Fig. 1(d). The $LiFePO_4$ crystallite appears as a dark region, while the amorphous carbon coating appears as a lightly shaded region. The image clearly shows a spacing of approximately 0.43 nm between the lattice strips, which is assigned to the (101) crystal face of $LiFePO_4$. The thickness of the carbon layer deposited on the surface of $LiFePO_4$/C was approximately 2 nm. Its carbon content was measured to be ~0.05 and 4.36 wt.% for bare $LiFePO_4$ and $LiFePO_4$/C, respectively. In general, electrode materials with uniform and thin low-carbon coatings are highly desired, as such materials have a high volumetric energy density and facilitate the penetration of lithium ions.[3] The materials prepared here are expected to meet these requirements. The tap density of $LiFePO_4$/C was calculated to be 1.2 g cm^{-3}, which is higher than that of previously synthesized nano-$LiFePO_4$ (<1.0 g cm^{-3}).[17]

Since the lithium ions in $LiFePO_4$ migrate through one-dimensional [010] channels, the electrochemical performance is significantly affected when the channels are blocked by defects created during particle formation. Reducing the

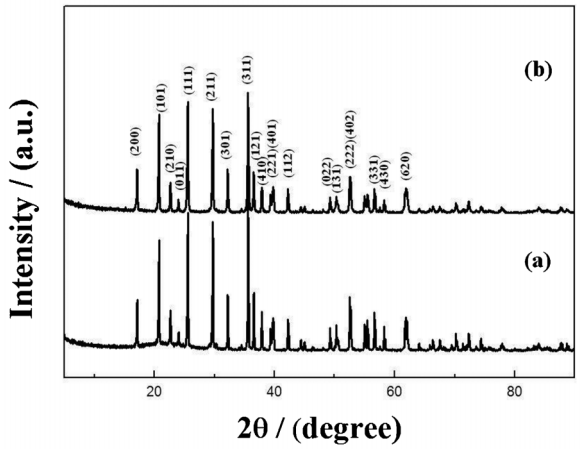

Fig. 2 XRD patterns for (a) bare $LiFePO_4$ and (b) $LiFePO_4$/C, where the mean crystallite size was calculated to be >100 and 66.5 nm, respectively, as calculated by the Scherrer equation.

concentration of these defects during synthesis is therefore essential. We conducted XRD and FTIR spectroscopy to investigate the generation of anti-site defects in the solvothermally prepared chelate-free $LiFePO_4$ microspheres employing ethanol as the solvent. Representative XRD patterns for bare $LiFePO_4$ and $LiFePO_4$/C are shown in Fig. 2. For $LiFePO_4$/C, all reflections are well indexed in the orthorhombic *Pnma* olivine structure without the presence of an impurity phase. The mean crystallite size of each sample was calculated using the Scherrer equation ($d = 0.9\ \lambda/\beta_{1/2}\ \cos\theta$) from the full width at half maximum (FWHM) of the (101), (111), (020), and (311) peaks. The mean crystallite sizes of bare $LiFePO_4$ and $LiFePO_4$/C were over 100 and 66.5 nm, respectively. The Rietveld refinement results and further detailed structural parameters for the samples are listed in Fig. S3† and Table S1.† The crystal lattice parameters and crystallite sizes of $LiFePO_4$ and $LiFePO_4$/C samples were smaller than those of $LiFePO_4$ prepared using a hydrothermal reaction (*i.e.*, <1% and 4.6%, respectively),[13] which is consistent with a decrease in anti-site defect concentration.

To further prove that the concentration of anti-site defects had decreased, we conducted FTIR analysis (Fig. 3(a)). The adsorption band of the natural P–O symmetric stretching vibration (*i.e.*, including defects) was assigned to the absorption occurring at approximately 1000 cm^{-1}, while that of defect-free $LiFePO_4$ was located at 957 cm^{-1} from theoretical calculations.[10] In our spectra, the P–O vibrations were shifted compared to the natural P–O vibration and were located at 968 and 961 cm^{-1}. Thus, these results are consistent with those obtained using ethylene glycol as the solvent and are approximate to the calculated values for defect-free $LiFePO_4$.[10,18] Combined with the observed unit cell volume reduction, the results thus indicate a decrease in $Fe^{\bullet}_{Li}$ anti-site defects in the crystal structure.

We then examined the valence state of iron in bare $LiFePO_4$ and $LiFePO_4$/C using XPS analysis (Fig. 3(b) and (c)), because Fe^{3+} salt was used as the starting material. Here it was observed that the Fe 2p and Fe 3s XPS spectra for bare $LiFePO_4$ and $LiFePO_4$/C were similar (hence, the spectra for bare $LiFePO_4$ are not shown). The Fe 2p spectra (Fig. 3(b)) are split into two main peaks (corresponding to Fe $2p_{3/2}$ and Fe $2p_{1/2}$) by spin–orbit coupling, which can be further subdivided into peaks at 709.6 and 711.2 eV, and "shake-up" satellite peaks at 724.3 and 728.3 eV.[19,20] Furthermore, an energy difference of ΔE = 5.7 eV corresponding to Fe^{2+} (ΔE of Fe^{3+} = ~6.5 eV) is observed for the two peaks in the Fe 3s spectrum (Fig. 3(c)). All

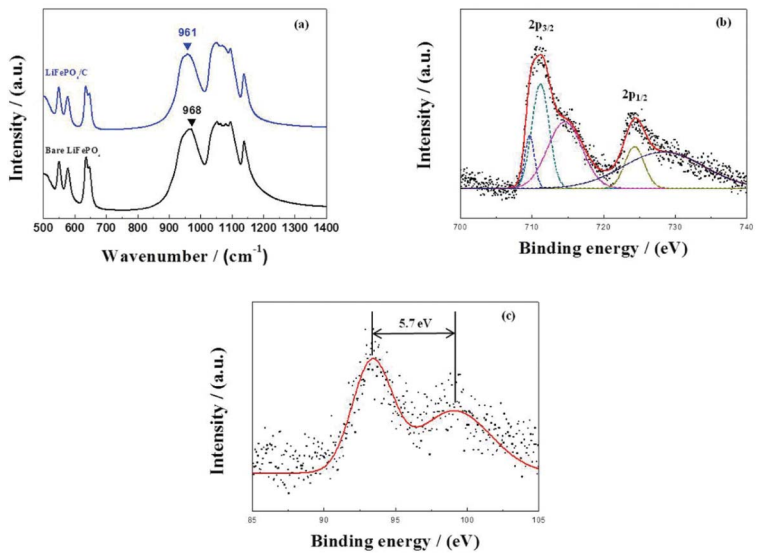

Fig. 3 (a) FTIR spectra for bare $LiFePO_4$ and $LiFePO_4$/C showing the reduction in anti-site defect concentration, as exemplified by the red shift. Note that the original P–O vibration is located at ~1000 cm^{-1} (see text). (b, c) XPS spectra of $LiFePO_4$/C focusing on (b) the Fe 2p spectrum, which is split into Fe $2p_{3/2}$ and Fe $2p_{1/2}$ peaks, and (c) the main peaks of the Fe 3s spectrum showing a difference of 5.7 eV. All peaks are characteristic of the Fe^{2+} valence.

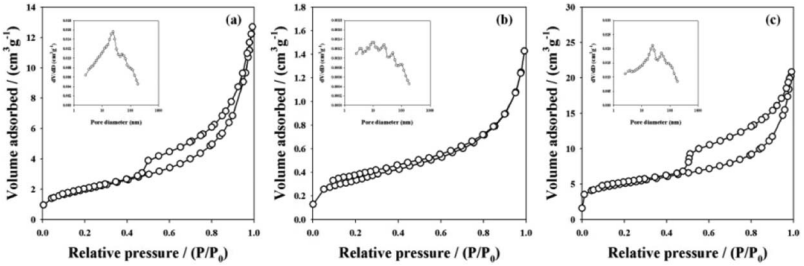

Fig. 4 Nitrogen adsorption–desorption isotherms for (a) the precursor, (b) bare $LiFePO_4$, and (c) $LiFePO_4$/C. The precursor and $LiFePO_4$/C show mesoporous structures associated with type IV curves, while bare $LiFePO_4$ has a solid structure associated with a type III curve (the insets show the pore-size distribution plots calculated by the Barrett–Joyner–Halenda equation).

spectra for Fe 2p and Fe 3s are consistent with the Fe^{2+} valence state.[20] Thus, despite the use of Fe^{3+} as the raw material, the predominant species is Fe^{2+}, and Fe^{3+} was readily reduced to the end product.

The pore-size distributions for the precursor, bare $LiFePO_4$, and $LiFePO_4$/C were measured using nitrogen adsorption and desorption (Fig. 4). Bare $LiFePO_4$ shows a type III isotherm because of its near-non-porous structure, with a specific surface area of only 1.2 $m^2\ g^{-1}$. In contrast, the precursor and $LiFePO_4$/C show type IV isotherms with large H2-type hysteresis, indicative of a mesoporous structure. The specific surface areas of the precursor and $LiFePO_4$/C were 7.2 and 17.7 $m^2\ g^{-1}$, respectively, while the mean pore sizes were 10.5 and 10.4 nm, respectively. Owing to citric acid pyrolysis during heat treatment,[15] the surface area of $LiFePO_4$/C was larger than that of the precursor.

Summarizing the preparation of $LiFePO_4$/C, its solvothermal synthesis using ethanol as the sole solvent exhibits the following advantageous characteristics: (i) a fast reaction time, (ii) the generation of highly crystalline micron-sized particles with a mesoporous spherical morphology without significant impurities, and (iii) the suppression of the occurrence of anti-site defects in the absence of a chelating agent. These characteristics are expected to give rise to an excellent electrochemical performance at high C-rates.

To investigate the electrochemical performance of bare $LiFePO_4$ and $LiFePO_4$/C, cyclic voltammetry measurements were conducted at a scan rate of 0.2 mV s^{-1} (Fig. 5(a)). Cyclic voltammetry measurements at various scan rates are shown in Fig. S4.† A single pair of sharp oxidation and reduction peaks, corresponding to the two-phase reaction of the Fe^{3+}/Fe^{2+} redox couple (*i.e.*, lithium insertion and extraction), can be clearly discerned.[21] For bare $LiFePO_4$, the oxidation and reduction peaks occur at 3.58 and 3.18 V, respectively, with the polarization being 0.4 V. For $LiFePO_4$/C, the oxidation and reduction peaks are located at 3.58 and 3.28 V, respectively, and the polarization is 0.3 V. The lower polarization and higher peak current (I_p) of $LiFePO_4$/C compared to that of bare $LiFePO_4$ can be attributed to the higher electronic conductivity and the improvement in lithium ion kinetics resulting from the carbon coating and the mesoporosity of the structure.[22] To obtain the apparent anodic and cathodic diffusion constants for both samples, we plotted the cathodic (I_{pc}) and anodic (I_{pa}) peak currents *versus* the square root of the scan rate, $v^{1/2}$, in the 0.2–1 mV s^{-1} range (inset of Fig. 5(a)). The diffusion constants for the Li^+ ions in the samples were calculated using the Randles-Sevcik equation:[23]

$$I_p/m = 0.4463F(F/RT)^{1/2}A_e(D_{app})^{1/2}C_{Li}{}^{*}v^{1/2} \quad (2)$$

where I_p is the peak current, m is the mass of the electrode, F is the Faraday constant, and A_e is the effective area of the electrode per unit mass. Here, it should be noted that $LiFePO_4$ has a one-dimensional diffusion path in the [010] plane, and A_e thus represents one-third of the total BET surface area of $LiFePO_4$, which is 1.2 $m^2\ g^{-1}$ for bare $LiFePO_4$ and 17.7 $m^2\ g^{-1}$ for $LiFePO_4$/C. Furthermore, D_{app} is the apparent diffusion constant for Li^+ ions, $C_{Li}{}^{*}$ is the Li^+ concentration in a particle before delithiation (0.0228 mol cm^{-3}), and v is the CV scan rate. The calculated cathodic and anodic apparent diffusion constants for bare $LiFePO_4$ were 4.5×10^{-15} and 7.1×10^{-15} $cm^2\ s^{-1}$, respectively, while $LiFePO_4$/C displayed values of 1.19×10^{-14} and 1.21×10^{-14} $cm^2\ s^{-1}$, respectively. These results indicate that the lithium diffusion constant for the $LiFePO_4$/C electrode was improved by the combined effect of the porous structure, the small crystallite size, the decreased concentration of $Fe^{\bullet}_{Li}$ anti-site defects, and the carbon coating of the $LiFePO_4$ particles.

Fig. 5(b) and (c) show the discharge curves for bare $LiFePO_4$ and $LiFePO_4$/C at various C rates, respectively. During charging and discharging, the cells were charged at a constant current of 0.1 C rate for each charging step and then discharged at progressively increasing C rates. At 0.1 C, the discharge capacities of bare $LiFePO_4$ and $LiFePO_4$/C were 27 and 153 mAh g^{-1}, respectively. As anticipated from the CV analysis, bare $LiFePO_4$ displays lower capacity than $LiFePO_4$/C because of the lower lithium diffusion constant and electronic conductivity. $LiFePO_4$/C exhibited a good rate performance with a capacity of 86 mAh g^{-1} at a relatively high rate of 20 C. Finally, $LiFePO_4$/C exhibited a high capacity of 140 mAh g^{-1} and an excellent cycling performance, with ~100% capacity retention after 50 cycles (Fig. 5(d)).

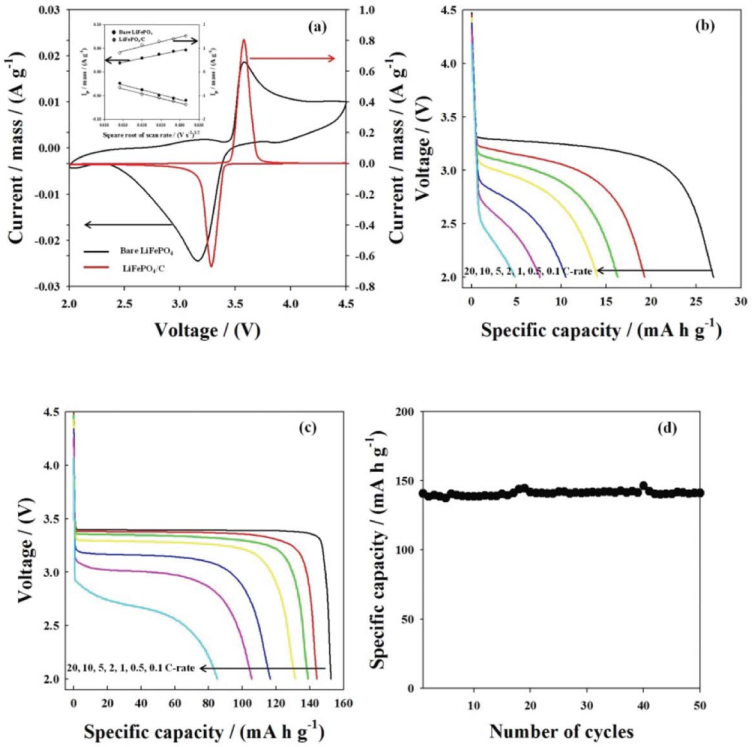

Fig. 5 (a) Cyclic voltammograms for bare $LiFePO_4$ and $LiFePO_4$/C at a scan rate of 0.2 mV s^{-1}. The inset shows a plot of the normalized peak current *versus* the square root of the scan rate. $LiFePO_4$/C displays a larger peak current and diffusion constant than bare $LiFePO_4$, as a result of its high porosity. Discharge curves for (b) bare $LiFePO_4$ and (c) $LiFePO_4$/C. A constant current was used for each charging step, while the discharge current was varied from 0.1 to 20 C rate. $LiFePO_4$/C displays increased discharge plateau voltages and capacities as compared to bare $LiFePO_4$, which results from its carbon coating and porous structure. (d) Cycling performance of $LiFePO_4$/C at a 1 C rate. A capacity of ~140 mAh g^{-1} and an excellent retention ratio of 100% is observed (determined by comparison of the capacity after one cycle with that after 50 cycles).

Conclusions

To improve the electrochemical performance of lithium iron phosphate ($LiFePO_4$) as a cathode material for lithium-ion batteries, we studied the solvothermal synthesis of carbon-coated $LiFePO_4$ in the absence of a chelating agent, using ethanol as the sole solvent. The as-synthesized carbon-coated $LiFePO_4$ particles display a uniform micron-sized spherical morphology with a mesoporous structure, containing less than 1% $Fe^{\bullet}_{Li}$ anti-site defects. The $LiFePO_4$ shows excellent rate performance (86 mAh g^{-1} at 20 C) and a high retention ratio (100% after 50 cycles at 1 C), making $LiFePO_4$ an attractive choice for the cathode material of small-scale lithium-ion batteries, and for medium- and large-scale applications such as in electric vehicles.

Acknowledgements

This work was supported by the Converging Research Center Program through the Ministry of Education, Science and Technology (2012K001257).

References

1 A. K. Padhi, K. S. Nanjundaswamy and J. B. Goodenough, *J. Electrochem. Soc.*, 1997, **144**, 1188.
2 A. S. Andersson, J. O. Thomas, B. Kalska and L. Häggström, *Electrochem. Solid-State Lett.*, 2000, **3**, 66.
3 J. Wang and X. Sun, *Energy Environ. Sci.*, 2012, **5**, 5163.
4 P. P. Prosini, M. Carewska, S. Scaccia, P. Wisniewski and M. Pasquali, *Electrochim. Acta*, 2003, **48**, 4205.
5 H. Huang, S. C. Yin and L. F. Nazar, *Electrochem. Solid-State Lett.*, 2001, **4**, A170.
6 H. Kim, H. Kim, S. W. Kim, K. Y. Park, J. Kim, S. Jeon and K. Kang, *Carbon*, 2012, **50**, 1966.
7 S. Y. Chung, J. T. Bloking and Y. M. Chiang, *Nat. Mater.*, 2002, **1**, 123.
8 C. Delacourt, P. Poizot, S. Levasseur and C. Masquelier, *Electrochem. Solid-State Lett.*, 2006, **9**, A352.
9 B. Kang and G. Ceder, *Nature*, 2009, **458**, 190.
10 X. Qin, J. Wang, J. Xie, F. Li, L. Wen and X. Wang, *Phys. Chem. Chem. Phys.*, 2012, **14**, 2669.
11 J. Chen and M. S. Whittingham, *Electrochem. Commun.*, 2006, **8**, 855.
12 J. Chen, S. Wang and S. Whittingham, *J. Power Sources*, 2007, **174**, 442.
13 F. Brochu, A. Guerfi, J. Trottier, M. Kopeć, A. Mauger, H. Groult, C. M. Julien and K. Zaghib, *J. Power Sources*, 2012, **214**, 1.

14 S. W. Oh, S. T. Myung, S. M. Oh, K. H. Oh, K. Amine, B. Scrosati and Y. K. Sun, *Adv. Mater.*, 2010, **22**, 4842.
15 J. Qian, M. Zhou, Y. Cao, X. Ai and H. Yang, *J. Phys. Chem. C*, 2010, **114**, 3477.
16 H. I. Chen and H. Y. Chang, *Colloids Surf., A*, 2004, **242**, 61.
17 C. Sun, S. Rajasekhara, J. B. Goodenough and F. Zhou, *J. Am. Chem. Soc.*, 2011, **133**, 2132.
18 W. Kang, C. Zhao, R. Liu, F. Xu and Q. Shen, *CrystEngComm*, 2012, **14**, 2245.
19 H. Liu, H. Yang and J. Li, *Electrochim. Acta*, 2010, **55**, 1626.
20 R. Dedryvère, M. Maccario, L. Croguennec, F. Le Cras, C. Delmas and D. Gonbeau, *Chem. Mater.*, 2008, **20**, 7164.
21 J. Yao, F. Wu, X. Qiu, N. Li and Y. Su, *Electrochim. Acta*, 2011, **56**, 5587.
22 J. K. Kim, J. Q. Choi, G. S. Chauhan, J. H. Ahn, G. C. Hwang, J. B. Choi and H. J. Ahn, *Electrochim. Acta*, 2008, **53**, 8258.
23 D. Y. W. Yu, C. Fietzek, W. Weydanz, K. Donoue, T. Inoue, H. Kurokawa and S. Fujitani, *J. Electrochem. Soc.*, 2007, **154**, A253.